npj | Computational Materials

www.nature.com/npjcompumats

ARTICLE OPEN

Charge disproportionation and site-selective local magnetic moments in the post-perovskite-type Fe_2O_3 under ultra-high pressures

Ivan Leonov[1,2], Gregory Kh. Rozenberg[3] and Igor A. Abrikosov[2,4]

The archetypal 3*d* Mott insulator hematite, Fe_2O_3, is one of the basic oxide components playing an important role in mineralogy of Earth's lower mantle. Its high pressure–temperature behavior, such as the electronic properties, equation of state, and phase stability is of fundamental importance for understanding the properties and evolution of the Earth's interior. Here, we study the electronic structure, magnetic state, and lattice stability of Fe_2O_3 at ultra-high pressures using the density functional plus dynamical mean-field theory (DFT + DMFT) approach. In the vicinity of a Mott transition, Fe_2O_3 is found to exhibit a series of complex electronic, magnetic, and structural transformations. In particular, it makes a phase transition to a metal with a post-perovskite crystal structure and site-selective local moments upon compression above 75 GPa. We show that the site-selective phase transition is accompanied by a charge disproportionation of Fe ions, with $Fe^{3\pm\delta}$ and $\delta \sim 0.05$–0.09, implying a complex interplay between electronic correlations and the lattice. Our results suggest that site-selective local moments in Fe_2O_3 persist up to ultra-high pressures of ~200–250 GPa, i.e., sufficiently above the core–mantle boundary. The latter can have important consequences for understanding of the velocity and density anomalies in the Earth's lower mantle.

npj Computational Materials (2019)5:90 ; https://doi.org/10.1038/s41524-019-0225-9

INTRODUCTION

Being model objects for studying the Mott transition phenomenon, the iron-bearing oxides play an important role in the mineralogy of Earth's lower mantle and outer core.[1–8] Because of their complex electronic, magnetic, and crystal structure behavior under high pressure–temperature conditions, these compounds have been of considerable recent interest.[6–12] It is known that upon compression these materials exhibit a magnetic collapse—a crossover from a high-spin (HS) to low-spin (LS) state of iron ions, resulting in drastic changes of their physical properties.[13–16] In fact, the anomalous behavior of their bulk modulus, density, and elastic properties is essential to understanding the seismic observations and dynamic processes in the Earth's lower mantle and outer core,[1–5] e.g., for interpretation of the anomalous seismic behavior at the bottom 400 km of Earth's mantle, in the so-called D″ region. The high-pressure electronic and structural properties of ferric oxide, hematite (α-Fe_2O_3), the "classical" example of a Mott-insulating material, is of particular interest for both fundamental science and technological applications. Its high-pressure properties, such as, rich allotropic behavior, release of oxygen resulting in the appearance of a homologous series of *n*FeO-*m*Fe_2O_3 oxides (with wüstite, FeO and Fe_2O_3 as the end-members), and the unclear role of Fe^{3+} in the nature and dynamics of the Earth's lower mantle have attracted much recent attention in geophysics and geochemistry.[6–8,10,17]

Under ambient conditions, Fe_2O_3 crystallizes in a rhombohedral corundum ($R\bar{3}c$ space group) crystal structure with Fe^{3+} cations located in distorted oxygen octahedra.[18,19] It is antiferromagnetic below ~260 K (Morin spin-flop transition temperature) and exhibits weak ferromagnetism (canted antiferromagnetism with a small net ferromagnetic moment of ~0.002μ_B) between 260 K and the Néel temperature of ~956 K.[18,19] Photoemission spectroscopy measurements show that Fe_2O_3 is a Mott-Hubbard insulator with a large energy gap of about 2.5 eV.[20–23] Upon compression above ~50 GPa Fe_2O_3 undergoes a sharp first-order phase transition to a metallic state (Mott insulator–metal transition) which is accompanied by a remarkable collapse of the lattice volume by about 10%.[6,10,12,24–30] The phase transition has been generally assigned to a HS to LS crossover of Fe^{3+} ions,[11] with a complex coexistence (with equal relative abundance) of the non-magnetic and HS components in the Mössbauer spectra at pressures above 50 GPa.[7,12] It was shown that the transition is accompanied by a structural transformation to the high-pressure crystal structure of Fe_2O_3. The latter was previously assigned either to an orthorhombic perovskite[24] or a Rh_2O_3-II-type crystal structure (*Pbcn*).[10,25] Only recently, based on single-crystal diffraction, the lattice structure has been resolved to be a distorted double-perovskite $GdFeO_3$-type (DPv) structure (space group $P2_1/n$).[7,12,31] Furthermore, the fine details of this phase transition seem to depend very much on "thermal prehistory" of a sample, showing that the Rh_2O_3-II-type structure may appear upon heating to about 1800 K with subsequent quenching to low temperatures.[7] Upon further compression above ~72 GPa, DPv-type Fe_2O_3 makes a transition to a new high-pressure polymorph whose crystal structure still remains controversial, with two

[1]M.N. Miheev Institute of Metal Physics, Russian Academy of Sciences, 620137 Yekaterinburg, Russia; [2]Materials Modeling and Development Laboratory, National University of Science and Technology 'MISIS', 119049 Moscow, Russia; [3]School of Physics and Astronomy, Tel Aviv University, 69978 Tel Aviv, Israel and [4]Department of Physics, Chemistry and Biology (IFM), Linköping University, SE-58183 Linköping, Sweden
Correspondence: Ivan Leonov (ivan.v.leonov@yandex.ru) or Igor A. Abrikosov (igor.abrikosov@liu.se)

Received: 29 September 2018 Accepted: 31 July 2019
Published online: 04 September 2019

proposed candidates: either a $CaIrO_3$-type post-perovskite (PPv) or orthorhombic *Aba*2 structures.[7,12,31,32]

Whereas the electronic properties of the low-pressure corundum ($R\bar{3}c$) phase of Fe_2O_3 are now well understood from, e.g., the LDA+U method[33,34] (LDA+U: density functional theory calculations within the local density approximation plus Hubbard U approach) or the DFT+DMFT calculations[35–41] (DMFT: dynamical mean-field theory of correlated electrons), the high-pressure properties of Fe_2O_3, e.g., its electronic structure, complex coexistence of the HS and LS states observed in the Mössbauer spectroscopy, a rich variety of structural polymorph, and details of the phase diagram in the megabar pressure range still remain enigmatic.[6–8,10,24–29,31,32] Very recently Greenberg et al.[12] detailed the pressure-induced Mott transition in the DPv-type Fe_2O_3 at about 50 GPa. In our present work, we extend this study focusing on a long-standing challenge of the electronic and magnetic properties of Fe_2O_3 under ultra-high pressures. We provide a microscopic theory of the high-pressure electronic structure and magnetic state of Fe_2O_3 up to compression above the core–mantle boundary conditions. Our results reveal that above 75 GPa Fe_2O_3 adopts a post-perovskite crystal structure, which is characterized by site-selective local moments, with local moments on half of the Fe sites collapsed into the LS state. The Fe 3d electrons on the rest of the Fe sites remain localized in a HS ($S = 5/2$) state up to ultra-high pressures of ~200–250 GPa, well above the core–mantle boundary. We predict that the site-selective local-moments phase is accompanied by a charge disproportionation of Fe ions, with $Fe^{3\pm\delta}$ and $\delta \sim 0.05$–0.09, implying a complex interplay between electronic correlations and the lattice.

RESULTS AND DISCUSSION

We employ a state-of-the-art fully self-consistent in charge density DFT + DMFT approach[35–40,42–46] to compute the electronic structure, magnetic state, and crystal structure properties of Fe_2O_3 under pressure. Our results for the calculated enthalpy (with the HS $R\bar{3}c$ phase taken as a reference) are summarized in Fig. 1. The pressure-induced evolution of the instantaneous local moments is shown in Fig. 2. Overall, the calculated electronic and lattice properties of Fe_2O_3 agree well with available experimental data. In agreement with previous studies,[11,12] at ambient pressure, we obtain a Mott-insulating solution with a large energy gap of ~2.5 eV (see Supplementary Fig. 1). The calculated local magnetic moment is ~4.8μ_B, clearly indicating that at ambient pressure the Fe 3d electrons are strongly localized and form a HS $S = 5/2$ state (Fe^{3+} ions have a $3d^5$ configuration with three electrons in the t_{2g} and two in the e_g orbitals). Our results for the equilibrium lattice constant $a = 5.61$ a.u. and bulk modulus K_0 ~ 187 GPa (with $K' \equiv dK/dP$ fixed to 4.1) are in good quantitative agreement with experiment.[7,12] Under pressure the energy gap gradually decreases, resulting in a Mott insulator to metal phase transition (MIT), within the $R\bar{3}c$ structure at about 72 GPa, upon compression to below $V \simeq 0.74V_0$. Indeed, our results for the Fe 3d spectral function of $R\bar{3}c$ Fe_2O_3 clearly reveal a sharp increase of the Fe 3d density of states at the Fermi level, associated with the Mott MIT (see Supplementary Fig. 2). The phase transition is accompanied by a HS–LS transition, with all the Fe^{3+} ions collapsed to a LS state.[11] This, however, cannot explain a complex coexistence of the HS and LS Fe^{3+} state near the MIT at pressures above 50 GPa found in the Mössbauer experiments (see refs [7,12] and references therein). In addition, the calculated critical pressure of MIT ~72 GPa is significantly higher, by ~40%, than that found in the experiments.[10,12] This manifests crucial importance of the interplay of the electronic state and lattice near the Mott transition in Fe_2O_3. In fact, it is known experimentally that the MIT in Fe_2O_3 is accompanied by a structural transformation to a double-perovskite $GdFeO_3$-type or Rh_2O_3-II-type (*Pbcn*) structure above ~50 GPa.

We compute the crystal structure phase stability and the electronic structure of the DPv and Rh_2O_3-II-type Fe_2O_3. To explore the phase stability of Fe_2O_3 near the Mott transition, we use the atomic positions and the crystal structure parameters taken from the experiments at about 50 GPa.[7,12] We use the DFT+DMFT approach with two (inequivalent) impurity sites in the unit cell in order to treat electron correlations in the Fe 3d bands of the structurally distinct Fe A (which have a prismatic oxygen coordination) and Fe B (octahedral) sites of the DPv, as well as of the PPv phase. We note that the DPv phase of Fe_2O_3 (monoclinic space group $P2_1/n$) adopts a general formula $A_2B'B''O_6$, i.e., it contains two crystallographically nonequivalent Fe B

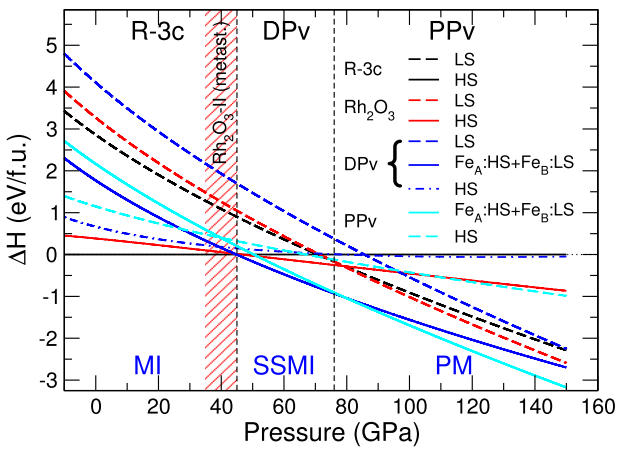

Fig. 1 Enthalpy difference (relative to the high-spin $R\bar{3}c$ solution) of paramagnetic Fe_2O_3 calculated by DFT + DMFT as a function of pressure for different phases at $T = 1160$ K. MI stands for Mott insulator; SSMI site-selective MI, PM paramagnetic metal. Above ~45 GPa, the corundum $R\bar{3}c$ (MI) phase transforms to the double-perovskite DPv (SSMI) phase which above 75 GPa further collapses to the post-perovskite PPv (PM) phase. The corresponding phase transitions are shown by vertical dashed lines. $Fe_{A/B}$ are structurally distinct prismatic/octahedral iron sites within the DPv and PPv crystal structures. The metastable Rh_2O_3-II phase is marked by red shading

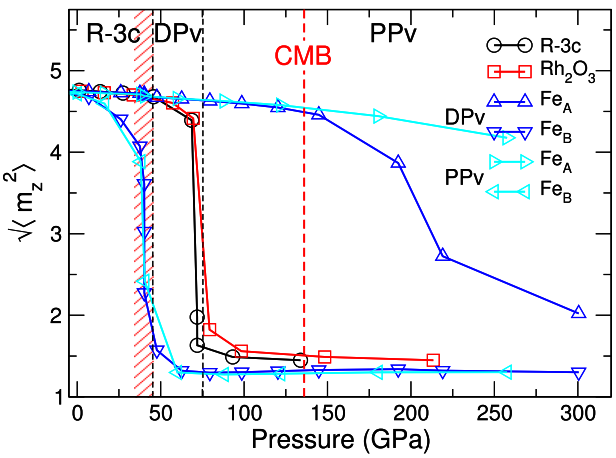

Fig. 2 Local magnetic moments $\sqrt{\langle \hat{m}_z^2 \rangle}$ of paramagnetic Fe_2O_3 evaluated for different phases within DFT + DMFT as a function of pressure. At high compression, the Fe 3d electrons show a complex coexistence of the localized (HS) and delocalized (LS) states, implying a site-selective localized to itinerant moment crossover under pressure. The metastable Rh_2O_3-II-type phase is marked by red shading. Note that site-selective local moments in PPv Fe_2O_3 persist up to a high pressure of ~200–250 GPa, well above the core–mantle boundary (CMB)

sites (with octahedral oxygen coordination). Our DFT+DMFT calculations with explicit treatment of the crystallographically different Fe A, B', and B'' sites (three-site impurity problem within DMFT) show that the Fe B' and B'' ions have very similar electronic state: similar spectral functions (in the local coordinate system), occupations, and local magnetic moments. Because of this we average the Green's functions corresponding to the Fe B' and B'' sites in our total energy calculations and solve two-site impurity problem within DMFT (one for the Fe A and one for the averaged Fe B site).

In agreement with experiment, the $R\bar{3}c$ phase is found to be energetically favorable at ambient pressure, with a total energy difference of about 670 and 350 meV/f.u. between corundum and the DPv, and corundum and the Rh_2O_3-II-type structures, respectively. Our results show that above ~45 GPa (upon compression below ~$0.84V_0$), Fe_2O_3 undergoes a phase transition from corundum to the double-perovskite DPv crystal structure (see Fig. 1). The Rh_2O_3-II lattice is energetically unfavorable, i.e., thermodynamically unstable, with a total energy difference with respect to the DPv phase of $\Delta E \sim 42$ meV/f.u. for $V = 0.84V_0$. Our result therefore suggests that at high temperatures the Rh_2O_3-II-type crystal structure can become metastable prior to the transition to the high-pressure DPv Fe_2O_3, in agreement with recent experiments.[7,31] Interestingly, both the $R\bar{3}c$ and Rh_2O_3-II phases exhibit a Mott MIT, accompanied by the HS–LS transition near 72 GPa. Most importantly, the $R\bar{3}c$-to-DPv phase transition is found to take place at ~45 GPa, in quantitative agreement with experiment.[7,12] This clearly demonstrates the crucial importance of the interplay of electronic correlations and the lattice to explain the properties of Fe_2O_3. The phase transition is accompanied by a collapse of the lattice volume by ~11.6%, whereas the calculated bulk modulus of the DPv phase (~259 GPa) is found to be substantially larger than that obtained for the HS state of the $R\bar{3}c$ phase (187 GPa).

Furthermore, we examine the high-pressure electronic structure and phase stability of paramagnetic Fe_2O_3 in the orthorhombic $Aba2$ and the $CaIrO_3$-type post-perovskite (PPv) crystal structures, i.e., for the two structural candidates for the high-pressure metallic phase proposed from experiment.[7,12,31] Our total energy calculations within a single-site DFT + DMFT method for the $Aba2$ phase reveal its remarkable thermodynamic instability (as high as ~3.71 eV/f.u. above the PPv phase). We note that while this value is large, ~740 meV/atom, it is not unrealistic. Here, we refer to two new metastable phases of SiO_2, coesite-IV and coesite-V, which have been synthesized experimentally.[47] The phases are energetically highly unfavorable—at 38 GPa, where coesite-V and coesite-IV are nearly degenerate in enthalpy in theoretical calculations, the calculated enthalpy difference between them and the ground state was found to be ~390 meV/atom. The values calculated for carbon polymorphs, for example, such as diamond and C_{60} are even higher. DFT + DMFT calculations with different computational parameters (U and J) show that the obtained result is robust, suggesting that $Aba2$ Fe_2O_3 is metastable at high pressures. Our result agrees well with recent X-ray diffraction studies which reveal that the $Aba2$ phase is in fact metastable with a stability range limited to low temperatures.[7] Moreover, the latter is experimentally found to transform into the PPv structure upon annealing to high temperatures.[7] Interestingly, the crystal structure analysis of the $Aba2$ structure of Fe_2O_3 reveals the existence of two sufficiently different Fe–Fe bond distances: the Fe–Fe pairs with a short inter-atomic distance of ~2.43 Å and the rest with that of 2.73 Å. While the $Aba2$ phase is non-magnetic (according to the low-temperature Mössbauer spectroscopy[12]), this may suggest dimerization of the Fe–Fe ions in $Aba2$ Fe_2O_3. As a consequence, it implies a possible importance of non-local correlation effects to explain the appearance of the metastable $Aba2$ phase at low temperatures. Based on our theoretical results, we predict a structural phase transition from the DPv to PPv phase

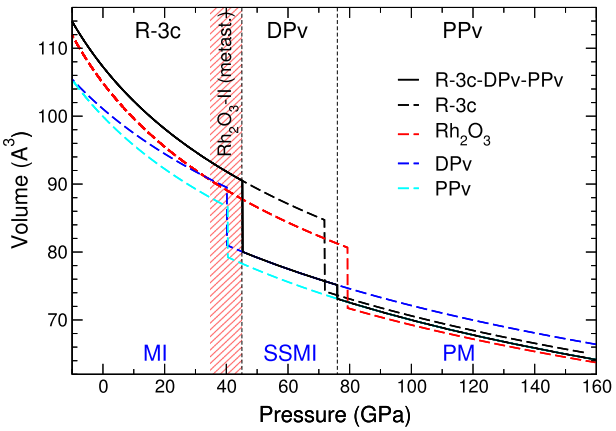

Fig. 3 Equation of state of Fe_2O_3 calculated by DFT + DMFT for different phases at $T = 1160$ K. Fe_2O_3 undergoes the corundum ($R\bar{3}c$) to double-perovskite (DPv) phase transition at about 45 GPa, and then above 75 GPa, it makes a DPv–PPv transformation (PPv post-perovskite). MI stands for Mott insulator, SSMI for site-selective MI, and PM for paramagnetic metal. The metastable Rh_2O_3-II-type phase is marked by red shading

above ~75 GPa, in quantitative agreement with available experiments.[7,12] The phase transition is accompanied by about 2.6% collapse of the lattice volume and is associated with formation of a metallic state (both Fe A and B sublattices are metallic). In Fig. 3 we summarize our results for the equation of state of the Fe_2O_3 polymorphs considered in the present study, revealing two distinct anomalies at about 45 and ~75 GPa.

Our results for the local magnetic moments and spectral properties confirm that a structural transition from the low-pressure corundum $R\bar{3}c$ to the DPv structure is accompanied by a Mott insulator to site-selective MI phase transition, in agreement with recent experiments.[12] In fact, the phase transition above 45 GPa is characterized by a collapse of local moments and emergence of a metallic state only on half of the Fe sites (see Fig. 2 and Supplementary Figs 3 and 4). The spectral function of the Fe B ions exhibits a large increase of its weight at the Fermi level for $V < 0.85V_0$, whereas the Fe A spectral weight at ε_F remains unchanged down to ~$0.6\,V/V_0$. That is, the prismatic Fe A sites remain insulating with the local magnetic moment of ~$4.6\mu_B$ (HS, $S = 5/2$), which is substantially larger than that for the Fe B sites $0.89\mu_B$ (LS, $S = 1/2$) at about 70 GPa. The HS–LS transition of the Fe A electrons in DPv Fe_2O_3 is found to occur at a substantially higher compression of ~$0.6V_0$, above 192 GPa, and is accompanied by ~5% collapse of the lattice volume. The latter transition is associated with a formation of a fully metallic state of the DPv Fe_2O_3 phase, where both the Fe A and B sublattices are metallic.

Our calculations show that Fe_2O_3 in the PPv phase exhibits a site-selective local moments behavior similar to that found in the SSMI DPv phase with the local magnetic moment of ~$4.58\mu_B$ for the Fe A sites (with prismatic oxygen coordination), which is substantially larger than that for the octahedral Fe B sites ~$0.97\mu_B$, around 88 GPa (see Fig. 2). Our calculations predict that site-selective local moments within the PPv phase persist up to a very high compression of ~200–250 GPa. That is, even at pressures near the core–mantle boundary (~140 GPa) Fe_2O_3 remains highly (para-) magnetic. The latter is particularly remarkable because both the prismatic Fe A and the octahedral Fe B sublattices are metallic. Moreover, analysis of the local (dynamical) spin-spin correlation function $\chi(\tau) = \langle \hat{m}_z(\tau)\hat{m}_z(0)\rangle$ of the DPv and PPv Fe_2O_3 shown in Fig. 4 reveals that in both phases the Fe A electrons are localized to form fluctuating moments [$\chi(\tau)$ is seen to be almost constant, independent of τ, and close to the unit], while the Fe B electrons are delocalized (itinerant-like). Our findings, therefore, suggest that the MIT in the DPv and PPv Fe_2O_3 under pressure is

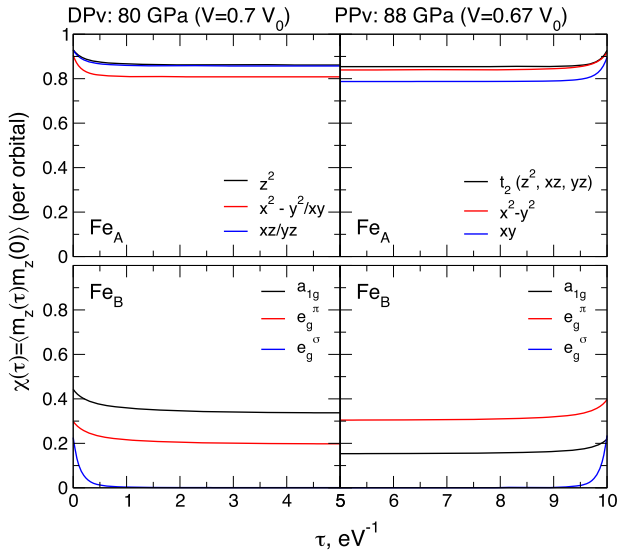

Fig. 4 Local spin susceptibility $\chi = \langle \hat{m}_z(\tau)\hat{m}_z(0)\rangle$ calculated by DFT + DMFT for the paramagnetic DPv (left panel) and PPv (right panel) phases of Fe_2O_3, for ~80 GPa (for the DPv phase) and 88 GPa (PPv), respectively. The Fe *A* electrons (associated with the prismatic Fe *A* sites) are localized to form fluctuating moments, while the octahedral Fe *B* sites are delocalized (itinerant-like). τ denotes the imaginary time, $\tau \in [0, \beta]$, where β is the inverse temperature, $\beta = 1/k_BT$

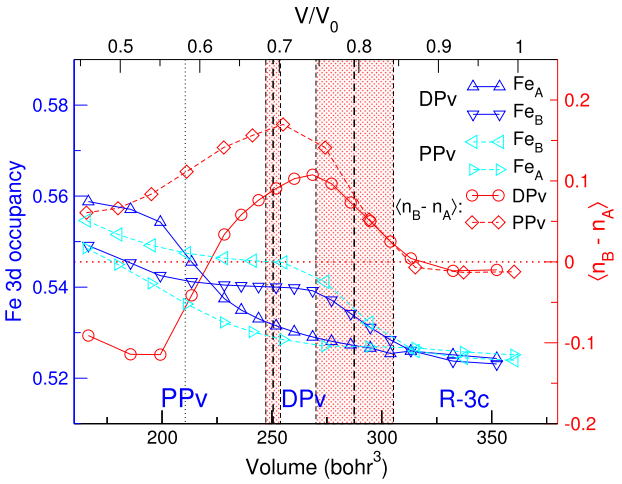

Fig. 5 Evolution of the Wannier Fe 3*d* total occupations and $Fe^{3\pm\delta}$ charge disproportionation with $\delta = (\langle \hat{n}_B\rangle - \langle \hat{n}_A\rangle)/2$ obtained by DFT + DMFT for the DPv and PPv phases as a function of volume. The $R\bar{3}c$–DPv and DPv–PPv phase transitions are shown by vertical dashed lines. Our results for the lattice volume collapse are marked by red shading. The SSMI–PM phase transition within the DPv crystal structure (at ~$0.58V_0$, corresponding to 192 GPa) is marked by a dotted line

associated with a site-selective delocalization of the Fe 3*d* electrons. We note that similar behavior associated with the crossover from a localized to itinerant state has recently been shown to appear at the pressure-induced Mott transition in monoxides MnO, FeO, CoO, and NiO.[14–16]

Our results provide a microscopic understanding of the complex coexistence of the HS and LS states observed in the high-pressure Mössbauer spectroscopy. In fact, this state can be rationalized as a site-selective Mott state of Fe_2O_3 in which local moments on half of the Fe sites collapse into the LS (metallic) state. Interestingly, our results suggest that the HS–LS state transition is accompanied by a remarkable enhancement of the crystal-field splitting (both in the DPv and PPv phases), caused by correlation effects (see Supplementary Fig. 5 and discussion there). We find that the crystal field energy splitting Δ_{cf} for the Fe 3*d* states (determined from the first moments of the interacting lattice Green's function) is larger for the small-moment Fe *B* sites with respect to the large-moment Fe *A* ions. Upon compression above the critical value, Δ_{cf} enhances by a factor of ~2, resulting in the site-selective HS–LS transformation. Moreover, our results show sufficiently different hybridization strength for the LS Fe *B* sites with respect to that in the HS Fe *A* site, which seems to mediate the critical value of the crystal-field splitting determined from the Hund's coupling *J* energy value (see Supplementary Fig. 6).

Interestingly, our results for both the DPv and PPv phases predict a charge disproportionation between the Fe *A* and *B* sites in Fe_2O_3. In Fig. 5 we show the total Fe *A* and *B* 3*d* occupations and $Fe^{3\pm\delta}$ 3*d* charge difference with $\delta \equiv \langle \hat{n}_B - \hat{n}_A\rangle/2$ as a function of volume. In particular, while it is seen to be negligible in the *conventional* Mott phase (MI) of the DPv and PPv Fe_2O_3 (i.e., it is absent even despite the fact that the *A* and *B* sites have very different oxygen environment, $\delta \sim 0$), the charge difference increases upon transition into the SSMI phase, and is about δ~0.05 and 0.09 for the DPv and PPv phases, respectively. Note that the charge disproportionation is absent in the $R\bar{3}c$ and Rh_2O_3-II phases (by symmetry all crystallographic positions of Fe are equivalent). Moreover, it is interesting to point out that the corresponding 3*d* charge difference (2δ=0.1–0.18) is in agreement with a charge disproportionation value of ~0.2 found in the low-temperature charge-ordered phases of the mixed-valent Fe-based oxides, such as Fe_3O_4 and Fe_2BO_4.[48–55]

We also notice that the sign of δ is opposite to what is expected: the small-volume octahedral Fe *B* cations, appear to hold more electrons than the prismatic Fe *A*, located in the largest oxygen cage. This behavior is a consequence of emptying of the antibonding e_g^σ states of the octahedral Fe *B* sites at the MI to SSMI phase transition, which leads to a different strength of covalent *p*–*d* bonding for the Fe *A* and *B* sites.[56] Moreover, upon further compression of the lattice below ~$0.6V_0$, above ~190 GPa, the charge disproportion is found to change sign upon transition to a (conventional) metallic state in the DPv phase. In the PPv Fe_2O_3 it tends to decrease below $\delta \sim 0.05$, implying a complex interaction between electronic correlations, local magnetism, and the lattice on microscopic level. We note that a similar behavior has been recently suggested to occur in nanocrystalline Fe_2O_3 under pressure.[57] In addition, we point out a similarity of the electronic and magnetic behavior of Fe_2O_3 to that observed in the rare-earth nickelates ($RNiO_3$ with R = Sm, Eu, Y, or Lu).[58–62] In fact, the latter exhibit a site-selective Mott transition, characterized by a two-sublattice symmetry breaking, with formation of site-selective local moments with localized Ni 3*d* magnetic moments and Ni-*d*–O-*p* singlet non-magnetic states. The localized Ni 3*d* moments are formed on the nickel sublattice having an increased mean Ni–O bond, while the non-magnetic states have a decreased Ni–O bond. Note that the nickelates remain insulating while exhibiting formation of site-selective local moments, in qualitative difference from a site-selective Mott-insulating state of Fe_2O_3. Moreover, a charge disproportionation between the local moment and Ni-*d*–O-*p* singlet sites is also small, 2δ = 0.1–0.16 electrons, in accordance with our result of ~0.1–0.18 for Fe_2O_3.[58,59] Because of this we suggest that charge disproportionation is the intrinsic property of the site-selective Mott phase of Fe_2O_3, which appears due to the complex interplay between electronic, magnetic, and lattice degrees of freedom. In fact, the LS state of Fe^{3+} ions experience more charge transfer from the ligands, resulting in a sufficient charge disproportionation between the HS and the LS states in the SSMI phase.

Overall, our calculations show that under pressure Fe_2O_3 undergoes a series of complicated electronic, magnetic, and structural transformations. It starts with a phase transition from the corundum to DPv phase at about 45 GPa, and then above 75 GPa, Fe_2O_3 makes a DPv–PPv transformation. All of these phase transformations are of first order, resulting in a substantial change of the lattice volume by ~2.6–11.6% (see Fig. 3). Our calculations reveal a complex interplay of electronic correlations and the crystal structure near the Mott transition, resulting in the formation of a site-selective Mott-insulating phase and site-selective collapse of the local moments. Below a megabar, our results show a remarkable competition of different crystallographic phases of Fe_2O_3, suggesting the importance of metastable phases for understanding its crystallochemistry. Most importantly, our results predict that site-selective local moments in the metallic PPv Fe_2O_3 persist up to ultra-high compression of ~200–250 GPa, i.e., well above the core-mantle boundary pressure. This, in fact, can be important for the understanding of the velocity and density anomalies in the Earth's lower mantle, providing a possible explanation for the origin of large low-shear-velocity provinces.

In conclusion, we show that the interplay between electronic correlations and the lattice in the vicinity of a Mott transition results in the formation of complex electronic and magnetic states in Fe_2O_3. This gives rise to a remarkable structural complexity of Fe_2O_3, implying a possible importance of metastable structures for understanding its high-pressure and high-temperature behavior. Our results explain microscopically the coexistence of the HS and LS states observed in Mössbauer spectroscopy at high pressures, suggesting the existence of a novel class of Mott systems—with site-selective local moments—which may have important impact for understanding the properties and evolution of the Earth's lower mantle and outer core. We expect that the electronic and structural complexity of Fe_2O_3 under pressure revealed in this study, e.g., its complex allotropy and the presence of metastable phases may affect present geophysical and geochemical models.

METHODS

We have employed the DFT + DMFT approach to explore the electronic structure, local magnetic state of Fe^{3+} ions, and crystal structure stability of paramagnetic Fe_2O_3 under pressure using the DFT+DMFT method[42–46] implemented with plane-wave pseudopotentials.[63–65] We start by constructing the effective low-energy O 2*p*–Fe 3*d* Hamiltonian $\left[\hat{H}^{\mathrm{DFT}}_{\sigma,\alpha\beta}(k)\right]$ using the projection onto Wannier functions to obtain the *p*–*d* Hubbard Hamiltonian (in the density–density approximation)

$$\hat{H} = \sum_{k,\sigma} \hat{H}^{\mathrm{DFT}}_{\sigma,\alpha\beta}(k) + \frac{1}{2} \sum_{i,\sigma\sigma',\alpha\beta} U^{\sigma\sigma'}_{\alpha\beta} \hat{n}_{i,\alpha\sigma} \hat{n}_{i,\beta\sigma'} - \hat{H}_{\mathrm{DC}}, \quad (1)$$

where $\hat{n}_{i,\alpha\sigma}$ is the occupation number operator for the *i*th Fe site with spin σ and (diagonal) orbital indices α. For this purpose, for the partially filled Fe 3*d* and O 2*p* orbitals we construct a basis set of atomic-centered symmetry-constrained Wannier functions.[66–68] The Wannier functions are constructed using the scheme of refs: [67,68] the O 2*p* orbitals were constructed using Wannier functions defined over the full energy range spanned by the *p*–*d* band complex; the localized Fe 3*d* orbitals are constructed using the Fe 3*d* band set. All the calculations are performed in the local basis set determined by diagonalization of the corresponding Fe 3*d* occupation matrices. In order to solve the realistic many-body problem, we employ the continuous-time hybridization-expansion quantum Monte-Carlo algorithm.[69] The Coulomb interaction has been treated in the density–density approximation. The elements of the *U* matrix are parametrized by the average Coulomb interaction *U* and Hund's exchange *J* for the Fe 3*d* shell. For all the structural phases considered here we have used the same $U = 6$ eV and $J = 0.86$ eV values as was estimated previously.[11,12] The spin–orbit coupling was neglected in these calculations. Moreover, the *U* and *J* values are assumed to remain constant upon variation of the lattice volume. We employ the fully localized double-counting correction, evaluated from the self-consistently determined local occupations, to account for the electronic interactions already described by DFT, $\hat{H}_{DC} = U\left(N - \frac{1}{2}\right) - J\left(N_\sigma - \frac{1}{2}\right)$, where N_σ is the total Fe 3*d* occupation with spin σ and $N = N_\uparrow + N_\downarrow$. Here, we employ a fully self-consistent in charge density DFT + DMFT scheme in order to take into account the effect of charge redistribution caused by electronic correlations and electron–lattice coupling. The spectral functions were computed using the maximum entropy method.

We explore the structural stability of Fe_2O_3 up to a pressure of 300 GPa, and, in particular, the influence of electronic correlations on the structural transition(s) and the electronic state of iron ions. To this end, we adopt the crystal structure data for the corundum ($R\bar{3}c$), double-perovskite ($P2_1/n$), Rh_2O_3-II-type (*Pbcn*), post-perovskite (*Cmcm*), and orthorhombic (*Aba*2) structures taken from experiment,[7,12] and calculated enthalpy within DFT +DMFT. To compute pressure we fit the calculated total energies using the third-order Birch–Murnaghan equation of states separately for the low- and high-volume regions.

DATA AVAILABILITY

The data that support the findings of this study are available from the corresponding authors upon request.

CODE AVAILABILITY

The DFT+DMFT code employed in this study is available from the corresponding authors upon request.

ACKNOWLEDGEMENTS

We thank E. Greenberg, L. Dubrovinsky, and R. Jeanloz for valuable discussions. Theoretical analysis of structural properties was supported by the Russian Science Foundation (Project No. 18-12-00492). Support provided by the Swedish Research Council Project No. 2015-04391, the Swedish Government Strategic Research Areas in Materials Science on Functional Materials at Linköping University (Faculty Grant SFO-Mat-LiU No. 2009-00971) and the Swedish e-Science Research Centre (SeRC) is gratefully acknowledged. This research was supported in part by Israeli Science Foundation Grant #1189/14 and #1552/18.

AUTHOR CONTRIBUTIONS

I.L. performed the theoretical analysis; all the authors contributed to the interpretation of the data and to the writing of the manuscript.

ADDITIONAL INFORMATION

Supplementary information accompanies the paper on the *npj Computational Materials* website (https://doi.org/10.1038/s41524-019-0225-9).

Competing interests: The authors declare no competing interests.

Publisher's note: Springer Nature remains neutral with regard to jurisdictional claims in published maps and institutional affiliations.

REFERENCES

1. Lin, J.-F. et al. Spin transition of iron in magnesiowüstite in the Earth's lower mantle. *Nature* **436**, 377 (2005).
2. Mao, Z., Lin, J.-F., Liu, J. & Prakapenka, V. B. Thermal equation of state of lower-mantle ferropericlase across the spin crossover. *Geophys. Res. Lett.* **38**, L23308 (2011).
3. Wu, Z., Justo, J. F. & Wentzcovitch, R. M. Elastic anomalies in a spin-crossover system: ferropericlase at lower mantle conditions. *Phys. Rev. Lett.* **110**, 228501 (2013).
4. Lin, J.-F., Speziale, S., Mao, Z. & Marquardt, H. Effects of the electronic spin transitions of iron in lower mantle minerals: implications for deep mantle geophysics and geochemistry. *Rev. Geophys.* **51**, 244–275 (2013).
5. Buffett, B. A. Earth's core and the geodynamo. *Science* **288**, 2007–2012 (2000).
6. Shim, S.-H. et al. Electronic and magnetic structures of the postperovskite-type Fe_2O_3 and implications for planetary magnetic records and deep interiors. *Proc. Natl. Acad. Sci. USA.* **106**, 5508–5512 (2009).
7. Bykova, E. et al. Structural complexity of simple Fe_2O_3 at high pressures and temperatures. *Nat. Commun.* **7**, 10661 (2016).
8. Kupenko, I. et al. Magnetism in cold subducting slabs at mantle transition zone depths. *Nature* **570**, 102–106 (2019).

9. Imada, M., Fujimori, A. & Tokura, Y. Metal-insulator transitions. *Rev. Mod. Phys.* **70**, 1039–1263 (1998).
10. Pasternak, M. P. et al. Breakdown of the Mott-Hubbard state in Fe_2O_3: a first-order insulator-metal transition with collapse of magnetism at 50 GPa. *Phys. Rev. Lett.* **82**, 4663–4666 (1999).
11. Kuneš, J., Korotin, D. M., Korotin, M. A., Anisimov, V. I. & Werner, P. Pressure-driven metal-insulator transition in hematite from dynamical mean-field theory. *Phys. Rev. Lett.* **102**, 146402 (2009).
12. Greenberg, E. et al. Pressure-induced site-selective Mott insulator-metal transition in Fe_2O_3. *Phys. Rev. X* **8**, 031059 (2018).
13. Cohen, R. E., Mazin, I. I. & Isaak, D. G. Magnetic collapse in transition metal oxides at high pressure: implications for the Earth. *Science* **275**, 654–657 (1997).
14. Leonov, I. Metal-insulator transition and local-moment collapse in FeO under pressure. *Phys. Rev. B* **92**, 085142 (2015).
15. Leonov, I., Pourovskii, L., Georges, A. & Abrikosov, I. A. Magnetic collapse and the behavior of transition metal oxides at high pressure. *Phys. Rev. B* **94**, 155135 (2016).
16. Leonov, I., Ponomareva, A. V., Nazarov, R. & Abrikosov, I. A. Pressure-induced spin-state transition of iron in magnesiowüstite (Fe,Mg)O. *Phys. Rev. B* **96**, 075136 (2017).
17. Jackson, I. *Earth's Mantle: Composition, Structure and Evolution*. (Cambridge University Press, Cambridge, 1998).
18. Shull, C. G., Strauser, W. A. & Wollan, E. O. Neutron diffraction by paramagnetic and antiferromagnetic substances. *Phys. Rev.* **83**, 333–345 (1951).
19. Greedon, J. E. *Encyclopedia of Inorganic Chemistry* (John Wiley & Sons, New York, 1994).
20. Fujimori, A., Saeki, M., Kimizuka, N., Taniguchi, M. & Suga, S. Photoemission satellites and electronic structure of Fe_2O_3. *Phys. Rev. B.* **34**, 7318–7328 (1986).
21. Lad, R. J. & Henrich, V. E. Photoemission study of the valence-band electronic structure in Fe_xO, Fe_3O_4, and α-Fe_2O_3 single crystal. *Phys. Rev. B.* **39**, 13478–13485 (1989).
22. Kim, C.-Y., Bedzyk, M. J., Nelson, E. J., Woicik, J. C. & Berman, L. E. Site-specific valence-band photoemission study of α-Fe_2O_3. *Phys. Rev. B* **66**, 085115 (2002).
23. Gilbert, B., Frandsen, C., Maxey, E. R. & Sherman, D. M. Band-gap measurements of bulk and nanoscale hematite by soft x-ray spectroscopy. *Phys. Rev. B* **79**, 035108 (2009).
24. Olsen, J. S., Cousins, C. S. G., Gerward, L., Jhans, H. & Sheldon, B. J. A study of the crystal structure of Fe_2O_3 in the pressure range up to 65 GPa using synchrotron radiation. *Phys. Scr.* **43**, 327 (1991).
25. Rozenberg, G. K. et al. High-pressure structural studies of hematite Fe_2O_3. *Phys. Rev. B* **65**, 064112 (2002).
26. Badro, J. et al. Nature of the high-pressure transition in Fe_2O_3 hematite. *Phys. Rev. Lett.* **89**, 205504 (2002).
27. Ono, S., Funakoshi, K., Ohishi, Y. & Takahashi, E. In situ x-ray observation of the phase transformation of Fe_2O_3. *J. Phys. Condens. Matter* **17**, 269 (2005).
28. Ono, S. & Ohishi, Y. In situ X-ray observation of phase transformation in Fe_2O_3 at high pressures and high temperatures. *J. Phys. Chem. Solids* **66**, 1714–1720 (2005).
29. Ito, E. et al. Determination of high-pressure phase equilibria of Fe_2O_3 using the Kawai-type apparatus equipped with sintered diamond anvils. *Am. Mineral.* **94**, 205–209 (2009).
30. Sanson, A. et al. Local structure and spin transition in Fe_2O_3 hematite at high pressure. *Phys. Rev. B* **94**, 014112 (2016).
31. Bykova, E. et al. Novel high pressure monoclinic Fe_2O_3 polymorph revealed by single-crystal synchrotron X-ray diffraction studies. *High Press. Res.* **33**, 534–545 (2013).
32. Tuček, J. et al. Zeta-Fe_2O_3—a new stable polymorph in iron(III) oxide family. *Sci. Rep.* **5**, 15091 (2015).
33. Anisimov, V. I., Zaanen, J. & Andersen, O. K. Band theory and Mott insulators: Hubbard *U* instead of Stoner *I. I. Phys. Rev. B* **44**, 943–954 (1991).
34. Rollmann, G., Rohrbach, A., Entel, P. & Hafner, J. First-principles calculation of the structure and magnetic phases of hematite. *Phys. Rev. B* **69**, 165107 (2004).
35. Metzner, W. & Vollhardt, D. Correlated lattice fermions in $d=\infty$ dimensions. *Phys. Rev. Lett.* **62**, 324–327 (1989).
36. Georges, A., Kotliar, G., Krauth, W. & Rozenberg, M. J. Dynamical mean-field theory of strongly correlated fermion systems and the limit of infinite dimensions. *Rev. Mod. Phys.* **68**, 13–125 (1996).
37. Kotliar, G. et al. Electronic structure calculations with dynamical mean-field theory. *Rev. Mod. Phys.* **78**, 865–951 (2006).
38. Anisimov, V. I., Poteryaev, A. I., Korotin, M. A., Anokhin, A. O. & Kotliar, G. First-principles calculations of the electronic structure and spectra of strongly correlated systems: dynamical mean-field theory. *J. Phys. Condens. Matter* **9**, 7359 (1997).
39. Lichtenstein, A. I. & Katsnelson, M. I. Ab initio calculations of quasiparticle band structure in correlated systems: LDA++ approach. *Phys. Rev. B.* **57**, 6884–6895 (1998).
40. Kuneš, J. et al. Dynamical mean-field approach to materials with strong electronic correlations. *Eur. Phys. J. Spec. Top.* **180**, 5–28 (2009).
41. Leonov, I., Skornyakov, S. L., Anisimov, V. I. & Vollhardt, D. Correlation-driven topological fermi surface transition in FeSe. *Phys. Rev. Lett.* **115**, 106402 (2015).
42. Pourovskii, L. V., Amadon, B., Biermann, S. & Georges, A. Self-consistency over the charge density in dynamical mean-field theory: a linear muffin-tin implementation and some physical implications. *Phys. Rev. B* **76**, 235101 (2007).
43. Haule, K. Quantum Monte Carlo impurity solver for cluster dynamical mean-field theory and electronic structure calculations with adjustable cluster base. *Phys. Rev. B* **75**, 155113 (2007).
44. Amadon, B. et al. Plane-wave based electronic structure calculations for correlated materials using dynamical mean-field theory and projected local orbitals. *Phys. Rev. B* **77**, 205112 (2008).
45. Aichhorn, M. et al. Dynamical mean-field theory within an augmented plane-wave framework: assessing electronic correlations in the iron pnictide LaFeAsO. *Phys. Rev. B* **80**, 085101 (2009).
46. Leonov, I., Anisimov, V. I. & Vollhardt, D. Metal-insulator transition and lattice instability of paramagnetic V_2O_3. *Phys. Rev. B* **91**, 195115 (2015).
47. Bykova, E. et al. Metastable silica high pressure polymorphs as structural proxies of deep Earth silicate melts. *Nat. Commun.* **9**, 4789 (2018).
48. Wright, J. P., Attfield, J. P. & Radaelli, P. G. Charge ordered structure of magnetite Fe_3O_4 below the Verwey transition. *Phys. Rev. B* **66**, 214422 (2002).
49. Senn, M. S., Wright, J. P. & Attfield, J. P. Charge order and three-site distortions in the Verwey structure of magnetite. *Nature* **481**, 173 (2012).
50. Perversi, G. et al. Co-emergence of magnetic order and structural fluctuations in magnetite. *Nat. Commun.* **10**, 2857 (2019).
51. Radaelli, P. G. Orbital ordering in transition-metal spinels. *New J. Phys.* **7**, 53 (2005).
52. Leonov, I., Yaresko, A. N., Antonov, V. N. & Anisimov, V. I. Electronic structure of charge-ordered Fe_3O_4 from calculated optical, magneto-optical Kerr effect, and O *K*-edge x-ray absorption spectra. *Phys. Rev. B* **74**, 165117 (2006).
53. Jeng, H.-T., Guo, G. Y. & Huang, D. J. Charge-orbital ordering in low-temperature structures of magnetite: GGA+*U* investigations. *Phys. Rev. B* **74**, 195115 (2006).
54. Pontius, N. et al. Time-resolved resonant soft x-ray diffraction with free-electron lasers: femtosecond dynamics across the Verwey transition in magnetite. *Appl. Phys. Lett.* **98**, 182504 (2011).
55. Leonov, I., Yaresko, A. N., Antonov, V. N., Attfield, J. P. & Anisimov, V. I. Charge order in Fe_2OBO_3: an LSDA+*U* study. *Phys. Rev. B* **72**, 014407 (2005).
56. Kuneš, J. & Křápek, V. Disproportionation and metallization at low-spin to high-spin transition in multiorbital mott systems. *Phys. Rev. Lett.* **106**, 256401 (2011).
57. Ovsyannikov, S. V., Morozova, N. V., Karkin, A. E. & Shchennikov, V. V. High-pressure cycling of hematite α-Fe_2O_3: nanostructuring, in situ electronic transport, and possible charge disproportionation. *Phys. Rev. B* **86**, 205131 (2012).
58. Park, H., Millis, A. J. & Marianetti, C. A. Site-selective Mott transition in rare-earth-element nickelates. *Phys. Rev. Lett.* **109**, 156402 (2012).
59. Subedi, A., Peil, O. E. & Georges, A. Low-energy description of the metal-insulator transition in the rare-earth nickelates. *Phys. Rev. B* **91**, 075128 (2015).
60. Ruppen, J. et al. Optical spectroscopy and the nature of the insulating state of rare-earth nickelates. *Phys. Rev. B* **92**, 155145 (2015).
61. Seth, P. et al. Renormalization of effective interactions in a negative charge transfer insulator. *Phys. Rev. B* **96**, 205139 (2017).
62. Ruppen, J. et al. Impact of antiferromagnetism on the optical properties of rare-earth nickelates. *Phys. Rev. B* **96**, 045120 (2017).
63. Giannozzi, P. et al. QUANTUM ESPRESSO: a modular and open-source software project for quantum simulations of materials. *J. Phys. Condens. Matter* **21**, 395502 (2009).
64. Leonov, I. et al. Structural relaxation due to electronic correlations in the paramagnetic insulator $KCuF_3$. *Phys. Rev. Lett.* **101**, 096405 (2008).
65. Leonov, I., Korotin, D., Binggeli, N., Anisimov, V. I. & Vollhardt, D. Computation of correlation-induced atomic displacements and structural transformations in paramagnetic $KCuF_3$ and $LaMnO_3$. *Phys. Rev. B* **81**, 075109 (2010).
66. Marzari, N., Mostofi, A. A., Yates, J. R., Souza, I. & Vanderbilt, D. Maximally localized Wannier functions: theory and applications. *Rev. Mod. Phys.* **84**, 1419–1475 (2012).
67. Anisimov, V. I. et al. Full orbital calculation scheme for materials with strongly correlated electrons. *Phys. Rev. B* **71**, 125119 (2005).
68. Trimarchi, G., Leonov, I., Binggeli, N., Korotin, D. & Anisimov, V. I. LDA+DMFT implemented with the pseudopotential plane-wave approach. *J. Phys. Condens. Matter* **20**, 135227 (2008).
69. Gull, E. et al. Continuous-time Monte Carlo methods for quantum impurity models. *Rev. Mod. Phys.* **83**, 349–404 (2011).

Open Access This article is licensed under a Creative Commons Attribution 4.0 International License, which permits use, sharing, adaptation, distribution and reproduction in any medium or format, as long as you give appropriate credit to the original author(s) and the source, provide a link to the Creative Commons license, and indicate if changes were made. The images or other third party material in this article are included in the article's Creative Commons license, unless indicated otherwise in a credit line to the material. If material is not included in the article's Creative Commons license and your intended use is not permitted by statutory regulation or exceeds the permitted use, you will need to obtain permission directly from the copyright holder. To view a copy of this license, visit http://creativecommons.org/licenses/by/4.0/.

© The Author(s) 2019